Digital Intelligence PRESS

International Scientific Technical and Economic Research
https://doi.org/10.67541/istaer2624

Research Article Volume 4, Issue 3 (July 2026) Open Access

A Model for Identifying the Forms of Discarded Products and Assessing Their Redesign Potential Based on Deep Learning

Mingxiang Yang *

College of Arts, Shandong Jianzhu University, Jinan, Shandong, China

***Corresponding author:** Mingxiang Yang. Email: yangmingxiang10@outlook.com

Abstract

The high-value redesign of discarded products relies on an accurate assessment of their remaining structure and redesign potential. However, existing visual recognition methods struggle to handle product damage, deformation, and occlusion, and lack quantitative assessment methods for redesign value. To address these issues, this paper proposes an end-to-end deep learning joint model that simultaneously performs shape recognition and redesign potential assessment for discarded products. In the shape recognition branch, a multi-branch feature extraction structure and a deformation-robust attention mechanism are designed to capture features of distorted and missing areas. Additionally, a shape structure preservation loss and an edge contrast loss are introduced to enhance boundary segmentation ability. In the potential assessment branch, a three-element index system comprising structural reusability, material integrity, and shape modification freedom is constructed. The spatial topological relationships among components are encoded using graph neural networks, and a shape–potential joint embedding space is established through cross-modal fusion. Continuous potential scores and discrete levels are output in parallel. The model achieves dual-task joint optimization using gradient coordination and an uncertainty weighting strategy. Experiments on our self-built dataset of 12,847 images of discarded electronic products show that the proposed method achieves 66.2% mIoU and 61.4% mAP in the shape recognition task, which are 3.8 and 4.7 percentage points higher than those of Mask2Former, respectively. The local mIoU on damaged areas is improved by 10.7 percentage points to 57.6%. The Spearman rank correlation coefficient between the predicted potential and expert scoring is 0.812, and the mean absolute error is reduced to 0.106. This method provides a quantifiable intelligent decision-making tool for the re-design of discarded products.

Keywords

Redesign of discarded products; Shape recognition; Deep learning; Potential assessment; Graph neural network

Received: 09 Jun 2026; Revised: 03 Jul 2026; Accepted: 11 Jul 2026; Published: 16 Jul 2026

1. INTRODUCTION

In the context of escalating global resource consumption and the rapid increase in electronic waste, the redesign of discarded products and their high-value recycling have become crucial steps in the green transformation of the manufacturing industry [1]. Unlike traditional material recycling methods (such as crushing and smelting), the redesign approach emphasizes retaining the original structure or components of the product and reconfiguring, replacing, or upgrading their functions to give the discarded product a new life cycle [2],[3]. This strategy can significantly reduce raw material consumption and carbon emissions, while preserving the process value embedded in the original manufacturing process. However, current re-design practices heavily rely on engineers' experience-based judgment and manual disassembly assessment [4]. When dealing with a large number of diverse and damaged discarded products, it is difficult to achieve scalable and standardized potential screening. How to quickly and accurately identify which products have redesign value from the massive waste stream is the core bottleneck restricting industrial implementation.

In the field of computer vision, existing shape recognition methods are mainly designed for complete products. For example, general instance segmentation models achieve remarkable results in tasks such as autonomous driving and robot grasping [5],[6],[7]. However, discarded products present unique visual challenges: they often exhibit distorted shapes, local fractures, surface wear, and component loss — conditions that rarely appear in regular training data — leading to a sharp decline in the segmentation accuracy of existing models [8]. More critically, discarded products are often obscured by other waste or stacked in complex spatial configurations, further exacerbating the recognition difficulty [9]. although existing studies have attempted to introduce deformable convolutions or data augmentation to alleviate deformation issues, these methods are mostly targeted at uniform deformations in industrial inspection and lack specialized modeling capabilities for the random, non-rigid, and discontinuous damage patterns of discarded products [10],[11]. The robustness of recognition is far from meeting practical requirements.

In addition to the difficulty of shape recognition itself, the assessment of redesign potential is almost absent in both academia and industry. Currently, there is a lack of a quantifiable index system to support the decision-making problem of whether discarded products are suitable for redesign [12]. Designers often rely solely on subjective experience to judge factors such as the completeness of the product shell and the usability of interfaces, leaving them unable to systematically weigh structural reusability, material damage degree, and geometric freedom for form modification. Even after shape recognition, the identified components have not yet formed a semantic mapping for re-design value, that is, the model does not know whether a damaged shell can still become the framework of a new product after a small amount of cutting, nor does it know whether a specific interface on a motherboard will affect the overall functional reuse after damage. This “identification but unable to assess” gap makes it difficult for computer vision technology to truly integrate into the re-design workflow [13],[14],[15].

To address these issues, this paper proposes a joint model based on deep learning for the identification of discarded product shapes and the assessment of re-design potential, achieving end-to-end mapping from image input to potential decision-making. In terms of shape recognition, a multi-branch feature extraction structure and a shape-robustness attention mechanism are designed to specifically address the distortion, damage, and multi-scale issues of discarded products. A shape structure preservation loss and an edge contrast loss are constructed to enhance boundary characterization capabilities. In terms of potential assessment, a tri-element index system of structural reusability, material integrity, and form modification freedom is established, and graph neural networks are introduced to encode the spatial relationships and connection topologies between components, through cross-modal fusion to construct a shape-potential joint embedding space, and finally output continuous potential scores and discrete grades in parallel. The overall model uses gradient coordination and uncertainty weighting strategies to achieve dual-task joint optimization. Through a large number of experiments on a self-built waste electronic product dataset, the results show that the proposed method significantly outperforms existing mainstream methods in shape recognition accuracy, potential assessment consistency, and robustness to damage occlusion, verifying the engineering practical value of the model in re-design-assisted decision-making.

2. SHAPE RECOGNITION NETWORK AND ALGORITHM IMPROVEMENT FOR DISCARDED PRODUCT FORMS

In view of the common engineering realities of discarded products — such as distorted shapes (bending and twisting), local missing parts (damage and fracture), and mixed multi-scale components — this paper designs a multi-branch feature extraction structure. This structure consists of three parallel branches: the global context branch uses a dilated convolution pyramid to capture the large-scale shape layout; the local detail branch retains edge and texture information through high-resolution feature maps; the multi-scale receptive field branch uses convolution kernels of different sizes to adapt to the scale changes from large shells to micro connectors. The three sets of features are aggregated through an adaptive fusion module guided by spatial attention to form a representation with more discriminative ability for the shape of abandoned products. On this basis, this paper introduces a deformation robustness attention mechanism (Deform-Robust Attention, DRA) to enhance the model's adaptability to non-rigid deformations. DRA is based on standard self-attention and predicts a two-dimensional offset for each query position, enabling the key-value sampling points to dynamically migrate to the semantic corresponding regions with undistorted shapes [16],[17]. Let the input feature map be $\mathrm{X} \in \mathbb{R}^{H\times W\times C}$, where H, W, and C represent the height, width, and number of channels, respectively. For the output position p, the attention response is calculated as:

$$\mathrm{y}_p = \sum_{k=1}^{K} \mathrm{W}_k \cdot \mathrm{x}_{p+p_k+\Delta p_k} \cdot \mathrm{a}_k \tag{1}$$

In the formula, K represents the total number of sampling points, p_k is the preset grid offset, Δp_k is the deformation offset learned by separable convolution from the current feature, a_k is the corresponding attention weight, W_k is a learnable projection matrix, and x represents the value of the input feature at the corresponding sampling location. By end-to-end learning Δp_k, the network can adaptively avoid damaged and missing areas and correct the spatial misalignment caused by distortion.

To enhance the model's ability to depict the boundary of discarded products and suppress noise interference, this paper constructs an improved loss function composed of a shape structure preservation loss and an edge contrast loss [18],[19],[20]. The shape structure preservation loss acts in the feature space, forcing the feature representation of the deformed sample to be close to that of the undeformed reference sample and away from samples of other categories. Let the feature vector of the anchor sample i in the batch be f_i, its corresponding undeformed reference sample feature be f_i^+, the negative sample set be $\{\mathrm{f}_i^-\}$, then the shape structure preservation loss $\mathcal{L}_{\text{shape}}$ is defined as:

$$\mathcal{L}_{\text{shape}} = \frac{1}{N}\sum_{i=1}^{N}\left(\| \mathrm{f}_i - \mathrm{f}_i^+ \|_2^2 + \sum_{j\in \text{neg}(i)} \max(0, m - \| \mathrm{f}_i - \mathrm{f}_i^- \|_2^2)\right) \tag{2}$$

Here, N represents the number of batch samples, m is the boundary margin parameter, and $\text{neg}(i)$ indicates the index of samples that are of a different class from the anchor point. This term ensures that similarly deformed samples maintain a compact clustering structure in the feature space. The edge contrast loss $\mathcal{L}_{\text{edge}}$ directly supervises the network's prediction of morphological boundaries using a pixel-level contrastive learning paradigm. Let the true edge map be $\mathrm{E} \in \{0,1\}^{H\times W}$, and the predicted edge probability map be $\hat{\mathrm{E}}$. For any edge pixel u and non-edge pixel v, the edge contrast loss forces $\widehat{\mathrm{E}}_u$ to be significantly greater than $\widehat{\mathrm{E}}_v$, while aligning the predicted edge with the direction gradient histogram of the true edge. Its expression is:

$$\mathcal{L}_{\text{edge}} = -\frac{1}{|\mathcal{P}|}\sum_{u\in\mathcal{P}} \log \frac{\exp\left(\frac{\widehat{\mathrm{E}}_u}{\tau}\right)}{\sum_{v\in\mathcal{N}} \exp(\widehat{\mathrm{E}}_v/\tau)} + \lambda_{\text{grad}} \cdot \mathrm{KL}\left(\nabla\widehat{\mathrm{E}} \parallel \nabla \mathrm{E}\right) \tag{3}$$

In the formula, $\mathcal{P}$ represents the set of true edge pixels, $\mathcal{N}$ represents the set of non-edge pixels, τ is the temperature hyperparameter, ∇ denotes the gradient operator, $\mathrm{KL}(\cdot\parallel\cdot)$ is the KL divergence, and λ_{grad} is the balance coefficient of the gradient alignment term. The final total loss is $\mathcal{L}_{\text{total}} = \mathcal{L}_{\text{seg}} + \alpha\mathcal{L}_{\text{shape}} + \beta\mathcal{L}_{\text{edge}}$, where $\mathcal{L}_{\text{seg}}$ is the primary segmentation loss, and α and β are hyperparameters.

To verify the effectiveness of the proposed structure, this paper designs a systematic comparison with mainstream detection and segmentation networks. The comparison benchmarks include Mask R-CNN based on standard convolution, DCNv2 with deformable convolution, and Mask2Former based on Transformer [21],[22],[23]. All three are re-trained and tested on the same discarded product dataset. The comparison experiments control a uniform input resolution, optimizer, and learning rate scheduling strategy. The evaluation metrics are the mean intersection over union (mIoU) of morphological segmentation and the local mIoU on damaged areas. Additionally, the performance degradation slope of each model under increasing simulated deformation conditions is recorded to characterize the morphological robustness. All comparisons are conducted using five-fold cross-validation and the mean and standard deviation are reported to eliminate the deviation caused by random initialization.

3. RE-DESIGN THE POTENTIAL ASSESSMENT MODULE AND THE FEATURE INTEGRATION ARCHITECTURE

The core of redesign potential assessment lies in converting the abstract remanufacturing value of a product into calculable engineering indicators [24]. This paper first constructs a three-dimensional potential assessment index system: Structural reusability measures the proportion of components in the discarded product that still retain their complete spatial configuration and connection relationships, reflecting the feasibility of direct reuse or local modification; Material integrity describes the proportion of areas on the product surface without cracks, corrosion, or material peeling, correlating the reinforcement cost and life expectancy in the re-design process [25]; Morphological transformation freedom characterizes the degree of difference between the existing geometric contour of the product and the target re-design form, with a smaller difference resulting in fewer processes required for cutting, filling, or re-structuring. These three indicators respectively depict the re-design potential from the topological, material, and geometric orthogonal dimensions, and together form the supervisory signals for the subsequent assessment model.

To explicitly model the spatial dependency and functional correlation relationships between the components of the discarded product, this paper designs a component relationship encoding module based on graph neural networks [26],[27]. The instance segmentation results output by the form recognition network of the discarded product are transformed into a graph structure $\mathcal{G} = (\mathcal{V}, \mathcal{E})$, where the node set $\mathcal{V}$ contains each node v_i corresponding to a detected component, and its initial feature vector $\mathrm{h}_i^{(0)} \in \mathbb{R}^{D_v}$ is composed of the morphological features (area, compactness, Hu moments) of the component, position features (centroid coordinates, bounding box), and the semantic category embedding output by the recognition network. The edge set $\mathcal{E}$ is constructed based on the spatial adjacency relationship: if the intersection and union ratio of the bounding boxes of two components exceeds the threshold θ_{adj} or the Euclidean distance between the two components is less than 0.3 times the average size of the component, an undirected edge is established between them. Each edge e_{ij} carries the initial feature $\mathrm{e}_{ij} \in \mathbb{R}^{D_e}$, including the relative displacement vector, direction angle difference, and length ratio of the contact boundary. The graph neural network uses the graph attention network (GAT) framework for information transmission, and the node update rule of the l-th layer is:

$$\mathrm{h}_i^{(l+1)} = \sigma\left(\sum\nolimits_{j \in \mathcal{N}(i) \cup \{i\}} \alpha_{ij}^{(l)} \mathrm{W}^{(l)} \mathrm{h}_j^{(l)} + \sum\nolimits_{j \in \mathcal{N}(i)} \beta_{ij}^{(l)} \mathrm{V}^{(l)} \mathrm{e}_{ij}\right) \tag{4}$$

In the formula, $\mathcal{N}(i)$ represents the set of neighbor nodes of node i, $\sigma(\cdot)$ is the ReLU activation function, $\mathrm{W}^{(l)}$ and $\mathrm{V}^{(l)}$ are the learnable weight matrices of the l-th layer, used to transform node features and edge features respectively. The attention coefficient $\alpha_{ij}^{(l)}$ is calculated through the shared attention mechanism: $\alpha_{ij}^{(l)} = \mathrm{softmax}_j\left(\mathrm{LeakyReLU}\left(\mathrm{a}^{(l)T}[\mathrm{W}^{(l)}\mathrm{h}_i^{(l)} \parallel \mathrm{W}^{(l)}\mathrm{h}_j^{(l)}]\right)\right)$, where $\parallel$ represents vector concatenation, and $\mathrm{a}^{(l)}$ is the attention parameter vector. The edge feature fusion coefficient $\beta_{ij}^{(l)}$ adopts a similar structure, but is learned independently to capture the unique contribution of the connection structure between components. After $L = 3$ layers of message passing, the feature $\mathrm{h}_i^{(L)}$ of each node encodes its own morphological information and the structured association information from adjacent components.

After obtaining the component-level structured representation, this paper constructs a morphological-potential joint embedding space to achieve a nonlinear mapping from geometric morphological features to potential indicators. This module adopts a cross-modal fusion structure, integrating three heterogeneous information: the global feature map $\mathrm{F}_{\text{global}} \in \mathbb{R}^{H' \times W' \times C'}$ from the morphological recognition network, the component relationship features $\left\{\mathrm{h}_i^{(L)}\right\}$ from the graph neural network, and the scene-level statistical features (component quantity, area distribution entropy, aspect ratio variance coefficient). Specifically, $\mathrm{F}_{\text{global}}$ is first compressed into a global morphological vector $\mathrm{g}_{\text{morph}} \in \mathbb{R}^{C'}$ through global average pooling. At the same time, the component-level features undergo sorting-invariant maximum pooling and average pooling to obtain the global component relationship vector $\mathrm{g}_{\text{graph}} = \mathrm{MaxPool}(\{\mathrm{h}_i^{(L)}\}) \oplus \mathrm{AvgPool}(\{\mathrm{h}_i^{(L)}\}) \in \mathbb{R}^{2D_h}$, where D_h is the output dimension of the graph network, $\oplus$ represents vector concatenation. The scene statistical feature vector $\mathrm{s} \in \mathbb{R}^{D_s}$ is directly normalized and connected. After being projected to a unified dimension D_{joint} through independent fully connected layers, they are adaptively fused through a cross-modal attention layer:

$$\mathrm{z}_{\text{fused}} = \mathrm{LayerNorm}\left(\mathrm{g}'_{\text{morph}} + \mathrm{MultiHeadAttn}(\mathrm{g}'_{\text{morph}}, \mathrm{g}'_{\text{graph}}, \mathrm{g}'_{\text{graph}})\right) \tag{5}$$

Here, $\mathrm{g}'_{\text{morph}}$, $\mathrm{g}'_{\text{graph}}$ and s' represent the projected vectors. MultiHeadAttn uses the morphological vector as the query, the component relationship vector as the key, and the value (Value), enabling the model to dynamically focus on the structural information most relevant to the potential [28]. The fused vector $\mathrm{z}_{\text{fused}}$ is then integrated with the scene statistics vector s' through a gating mechanism: $\mathrm{z}_{\text{final}} = \gamma \odot \mathrm{z}_{\text{fused}} + (1-\gamma) \odot \mathrm{s}'$, where the gating vector $\gamma = \mathrm{sigmoid}(\mathrm{W}_{\text{gate}}[\mathrm{z}_{\text{fused}}; \mathrm{s}'])$ is adaptively learned by the network.

Finally, to simultaneously provide evaluation results for both continuous accuracy and discrete decision-making, this paper designs a parallel output structure for potential regression and level classification [29]. The regression branch outputs the three-dimensional potential vector $\hat{p} = [\hat{p}_{\text{struct}}, \hat{p}_{\text{mater}}, \hat{p}_{\text{form}}]^T \in [0,1]^3$, corresponding to the predicted values of structural reusability, material integrity, and morphological modification freedom. The classification branch discretizes the potential into high, medium, and low levels, and outputs the probability distribution $\hat{c} \in \Delta^3$. Both branches share the aforementioned z_{final} feature, and generate outputs through two independent two-layer multi-layer perceptrons. The regression loss uses an uncertainty loss that combines the absolute error and variance weighting [30]:

$$\mathcal{L}_{\text{reg}} = \frac{1}{3}\sum_{k=1}^{3}\left(\frac{|\, p_k - \hat{p}_k \,|}{2\sigma_k^2} + \frac{1}{2}\log\sigma_k^2\right) \tag{6}$$

Here, p_k represents the true value of the k-th potential indicator (obtained through expert annotation or mechanical simulation), and σ_k^2 represents the heteroscedastic noise predicted by the network for each indicator. This design enables the model to output an estimate of the uncertainty of the predicted values. The classification loss is the standard cross-entropy loss $\mathcal{L}_{\text{cls}} = -\sum_{k=1}^{3} c_k \log \hat{c}_k$, where c_k is the one-hot encoded version of the true rating label, and $\hat{c}_k$ is the predicted probability. The total evaluation loss is $\mathcal{L}_{\text{eval}} = \mathcal{L}_{\text{reg}} + \lambda_{\text{cls}}\mathcal{L}_{\text{cls}}$, where λ_{cls} is the balance coefficient. In the inference stage, the regression branch outputs continuous potential scores for fine sorting, and the classification branch outputs ratings for quick screening. Both can also be adaptively switched or weighted fused based on the product type.

4. OVERALL MODEL ARCHITECTURE AND TRAINING STRATEGY

The overall model proposed in this paper integrates the identification of discarded product forms and the assessment of re-design potential into an end-to-end dual-task joint learning framework, sharing the underlying feature extraction network and synchronously optimizing the objectives of both tasks. The model takes the discarded product image $I \in R^{H_0 \times W_0 \times 3}$ as input, and extracts multi-scale feature pyramids $\{P_2, P_3, P_4, P_5\}$ through the shared backbone network (a combination of ResNet-50 and the deformable robustness attention module). The morphology recognition head outputs instance segmentation results based on the feature pyramid, including component category labels $\hat{y}_{\text{cls}}$, bounding boxes $\hat{b}$, and pixel-level masks $\hat{M}$. The potential assessment head takes the segmentation results output by the recognition head and the shared features as input, and outputs potential regression values $\hat{p}$ and potential grades $\hat{c}$ through the graph neural network and cross-modal fusion module. The two tasks update the shared backbone network simultaneously during backpropagation, enabling the component boundaries and structural relationships learned by morphology recognition to directly serve potential assessment, while the supervision signal from potential assessment feeds back to morphology recognition, guiding the network to focus on the key components that significantly impact the redesign decision. Let the loss of the morphology recognition task be $\mathcal{L}_{\text{recog}} = \mathcal{L}_{\text{cls}} + \mathcal{L}_{\text{box}} + \mathcal{L}_{\text{mask}} + \mathcal{L}_{\text{shape}} + \mathcal{L}_{\text{edge}}$, and the loss of the potential assessment task be $\mathcal{L}_{\text{eval}} = \mathcal{L}_{\text{reg}} + \lambda_{\text{cls}}\mathcal{L}_{\text{cls}}^{\text{grade}}$. Then, the end-to-end joint loss function is:

$$\mathcal{L}_{\text{joint}} = \mathcal{L}_{\text{recog}} + \mathcal{L}_{\text{eval}} \tag{7}$$

This joint framework avoids the problem in traditional two-stage methods where identification errors accumulate and amplify in the evaluation stage, enabling the system to directly optimize the final evaluation accuracy [31],[32].

Due to the significant differences in the convergence speed and gradient scale between the morphological recognition and potential assessment tasks, simply adding them together may lead to the gradient-dominated task suppressing the optimization of the other task. Therefore, this paper introduces the strategy of gradient coordination between tasks and uncertainty weighting. Drawing on the idea of homoscedastic uncertainty in multi-task learning, noise parameters σ_{recog} and σ_{eval} are assigned for each task, and the joint loss is re-constructed as:

$$\mathcal{L}_{\mathrm{joint}}^{\mathrm{unc}} = \frac{1}{2\sigma_{\mathrm{recog}}^{2}}\mathcal{L}_{\mathrm{recog}} + \frac{1}{2\sigma_{\mathrm{eval}}^{2}}\mathcal{L}_{\mathrm{eval}} + \log\left(\sigma_{\mathrm{recog}}\sigma_{\mathrm{eval}}\right) \tag{8}$$

Among them, σ_{recog} and σ_{eval} are trainable parameters. The term $\log(\sigma_{\mathrm{recog}}\sigma_{\mathrm{eval}})$ serves as a regularization term to prevent noise parameters from growing infinitely. This mechanism enables the model to automatically balance the relative weights of the two tasks: the task that converges faster corresponds to a larger σ^2, thereby obtaining a smaller loss coefficient and avoiding it from dominating the gradient update. On this basis, a gradient coordination strategy is further adopted to dynamically cut the gradients returned from the shared main network. Let θ_{shared} be the shared parameters, and $\mathrm{g}_{\mathrm{recog}}$ be the gradient from the morphological recognition task, and $\mathrm{g}_{\mathrm{eval}}$ be the gradient from the potential evaluation task. If the angle between the two gradients is greater than $90°$ (i.e., the cosine similarity is negative), it indicates that there is a conflict between the two tasks in the current parameter space. At this time, the gradient is projected onto the direction of the angle bisector of the two gradients:

$$\mathrm{g}_{\mathrm{final}} = \begin{cases} \mathrm{g}_{\mathrm{recog}} + \mathrm{g}_{\mathrm{eval}}, & \cos(\mathrm{g}_{\mathrm{recog}}, \mathrm{g}_{\mathrm{eval}}) \geq 0 \\ \mathrm{g}_{\mathrm{recog}} + \mathrm{g}_{\mathrm{eval}} - \dfrac{\mathrm{g}_{\mathrm{recog}} \cdot \mathrm{g}_{\mathrm{eval}}}{\parallel \mathrm{g}_{\mathrm{eval}} \parallel^{2}} \mathrm{g}_{\mathrm{eval}}, & \text{otherwise} \end{cases} \tag{9}$$

In the formula, $\cos(\cdot,\cdot)$ represents the cosine similarity. This operation eliminates the opposing gradient components between tasks while maintaining the overall update direction, thereby enhancing the stability and convergence efficiency of multi-task learning.

To address the scarcity of damaged and occluded samples in the discarded product data, this paper designs a physically-inspired data augmentation strategy, including two categories: damage simulation and occlusion synthesis. Damage simulation is based on the finite element concept, generating random fracture paths on the instance mask of the complete product: first, extract the product's axis, generate fracture seed points along the axis with probability p_{crack}, and then partition the product area into several sub-blocks through Voronoi partitioning [33]. Let Ω be the original mask area, Ω' be the mask generated by damage simulation, satisfying $\Omega' = \Omega \setminus \bigcup_{k=1}^{K} \mathrm{Circle}(\mathrm{c}_k, r_k)$, where K is the number of damage areas, c_k is the kth damage center, and $r_k \sim \mathcal{U}(0.05\ell, 0.2\ell)$ is the damage radius, ℓ is the diagonal length of the product's outer rectangle. Occlusion synthesis randomly crops irregularly-shaped foreground objects (such as tools, labels, other waste) from the background image library and superimposes them onto the product area, simultaneously modifying the corresponding mask labels. Let Ω_{occ} be the occlusion mask, then the pixel value of the synthesized image is $\mathrm{I}_{\mathrm{syn}}(\mathrm{x}) = (1 - 1_{\Omega_{\mathrm{occ}}}(\mathrm{x})) \cdot \mathrm{I}(\mathrm{x}) + 1_{\Omega_{\mathrm{occ}}}(\mathrm{x}) \cdot \mathrm{I}_{\mathrm{obj}}(\mathrm{x})$, where $1_{\Omega_{\mathrm{occ}}}$ is the indicator function, and $\mathrm{I}_{\mathrm{obj}}$ is the occlusion object image. These two augmentation strategies can be used independently or in combination. Each training image is applied with damage simulation with a 50% probability, occlusion synthesis with a

50% probability, and both with a 30% probability simultaneously.

During the training and validation stages, a strict staged strategy is adopted to avoid overfitting and objectively evaluate the generalization ability [34]. The entire discarded product dataset (including N product types, with approximately 500-2000 instances per type) is divided into training set, validation set, and test set in a 7:1:2 ratio, ensuring that the same product instance does not appear across sets. The training stage is divided into three sub-stages: warm-up period, main training period, and fine-tuning period. The warm-up period lasts for 5 epochs, only training the shape recognition network, freezing the graph neural network and potential evaluation head, enabling the shared backbone and recognition branch to have basic component detection capabilities. The warm-up period uses a smaller learning rate of 1×10^{-4} and a batch size of 8. The main training period conducts complete end-to-end joint training for 80 epochs, using a cosine annealing schedule to reduce the learning rate from 5×10^{-4} to 1×10^{-6}, and simultaneously enabling the aforementioned uncertainty weighting and gradient coordination strategies. Every 10 epochs, the current model's shape recognition mIoU and potential regression MAE are evaluated on the validation set, and the checkpoint with the minimum validation loss is saved. The fine-tuning period reduces the learning rate to 1×10^{-6} in the last 10 epochs, only updating the parameters of the potential evaluation branch, keeping the shared backbone and recognition branch fixed, so that the evaluation branch can better adapt to the learned feature space. The evaluation metrics are designed to balance the performance and collaborative efficiency of the two tasks [35]. The shape recognition task uses the average intersection over union (mIoU), average bounding box accuracy (AP@0.5), and local intersection over union (local mIoU, calculated only on components overlapping more than 20% with the damaged area). The potential assessment task employs the mean absolute error (MAE) of regression tasks, the Spearman rank correlation coefficient (ρ, used to measure the consistency of ranking), and the three-class classification accuracy (Acc@3) of classification tasks. Additionally, the joint indicator $F_{\text{joint}} = \frac{2 \cdot \text{mIoU} \cdot \text{Acc@3}}{\text{mIoU} + \text{Acc@3}}$ is defined to comprehensively evaluate the end-to-end performance of the model. All indicators are reported as the mean and standard deviation on the test set, and the influence of randomness is eliminated through five independent runs.

5. EXPERIMENTAL DESIGN AND RESULT ANALYSIS

5.1 Dataset construction and annotation method

To verify the validity of the model proposed in this paper, the first image dataset for discarded electronic products in the redesign scenario was constructed. It covers four product categories: smartphones, notebook computer motherboards, small household appliances (electric shavers, hair dryers), and power adapters. There are a total of 12,847 images. The images were captured under various backgrounds and lighting conditions, including conveyor belt scenarios (45%), sorting table scenarios (35%), and simulated stacking scenarios (20%). Each image has a resolution of 1920×1080 pixels and was manually annotated: using the Polygon annotation tool to outline the contours of each disassemblable component pixel by pixel, assigning component category labels (a total of 21 categories, such as “shell”, “PCB”, “battery interface”, “heat sink”, etc.), and marking damaged areas (cracks, missing parts, perforations) and occluded areas. The annotation work was completed by 5 researchers with mechanical design backgrounds. Each image was independently annotated by at least two people, and any discrepancies were arbitrated by a third person. The acquisition of potential labels was achieved through a combination of expert scoring and finite element simulation: for structural reusability, 3 experts in the re-design field rated the completeness of component connection methods (clasps, screws, adhesives) on a 0-1 scale, and supplemented with discrete element simulation to evaluate the structural deformation energy after disassembly; for material integrity, the surface reflection spectrum of the product was extracted using a hyperspectral imager and combined with mechanical indentation tests to obtain the equivalent Young's modulus attenuation rate, normalized to the 0-1 range; for morphological modification freedom, the point cloud of the product was obtained using a 3D scanner and the Hausdorff distance between it and the standard parametric template was calculated, mapped to a 0-1 score after reverse transformation. The potential label of each image was a three-dimensional vector $\mathrm{p} = [p_{\mathrm{struct}}, p_{\mathrm{mater}}, p_{\mathrm{form}}]^T$, and the mean $\bar{p} = (p_{\mathrm{struct}} + p_{\mathrm{mater}} + p_{\mathrm{form}})/3$ was used as the basis for discrete level classification: $\bar{p} \geq 0.7$ was high potential (level 2), $0.4 \leq \bar{p} < 0.7$ was medium potential (level 1), and $\bar{p} < 0.4$ was low potential (level 0). The dataset was randomly divided into training (8,993 images), validation (1,285 images), and test (2,569 images) sets in a 7:1:2 ratio. The sample distribution for each category is shown in Table 1.

Table 1. Categories and sample distribution of the waste electronic products dataset

Product categories	Training set	Validation set	Test set	High potential ratio	The proportion of medium potential	Low potential ratio
Smartphones	2,481	354	709	0.32	0.45	0.23
Laptop computer motherboards	2,107	301	602	0.28	0.42	0.30
Small household appliances power adapter	2,536	362	724	0.41	0.38	0.21
In total	1,869	268	534	0.35	0.40	0.25
Product categories	8,993	1,285	2,569	0.34	0.41	0.25

5.2 Comparison experiment on morphological recognition accuracy

The morphological recognition network proposed in this paper (denoted as Ours-Seg) is compared with five mainstream methods: Mask R-CNN (ResNet-50-FPN), YOLACT, SOLOv2, Mask2Former (Swin-T), and DCNv2 (deformable convolution network). All the comparison models were trained from scratch on the same training set for 120 epochs. The optimizer used was SGD (momentum 0.9, weight decay 1e-4), with an initial learning rate of 0.01 and a multi-step decay (decreasing by 0.1 at epochs 60 and 90). The evaluation metrics selected were the mean average precision (mAP, with IoU thresholds ranging from 0.5 to 0.95 in increments of 0.05), the pixel-level average intersection over union (mIoU), and the local mIoU for damaged areas (only calculated for components overlapping with the damaged annotation area by more than 20%). Additionally, the component-level F1-score was introduced as a supplementary metric, defined as follows:

$$F1 = \frac{2 \cdot \mathrm{Precision} \cdot \mathrm{Recall}}{\mathrm{Precision} + \mathrm{Recall}}, \mathrm{Precision} = \frac{TP}{TP + FP}, \mathrm{Recall} = \frac{TP}{TP + FN} \tag{10}$$

In the formula, TP, FP, and FN represent the number of correctly detected components, the number of falsely detected components, and the number of missed detected components respectively. The criterion is that the IoU between the predicted mask and the ground truth mask exceeds 0.5. Table 2 presents the morphological recognition performance of each method on the test set.

Table 2. Performance comparison of different methods in the task of identifying abandoned product forms

Method	mAP@0.5:0.95 (%)	mIoU (%)	local mIoU (%)	F1-score (%)
Mask R-CNN	52.3 ± 1.2	58.7 ± 1.0	41.2 ± 1.5	64.1 ± 1.1
YOLACT	48.9 ± 1.5	54.2 ± 1.3	37.8 ± 1.8	59.3 ± 1.4
SOLOv2	53.1 ± 1.1	59.3 ± 0.9	42.5 ± 1.4	65.2 ± 1.0
Mask2Former	56.7 ± 1.0	62.4 ± 0.8	46.9 ± 1.3	68.5 ± 0.9
DCNv2	54.8 ± 1.3	60.1 ± 1.1	48.3 ± 1.6	66.7 ± 1.2
Ours-Seg	61.4 ± 0.9	66.2 ± 0.7	57.6 ± 1.2	72.8 ± 0.8

From the data in Table 2, it can be seen that the method proposed in this paper achieves the best results in all four indicators. The mAP reaches 61.4%, which is 4.7 percentage points higher than the second-best Mask2Former (56.7%). Particularly noteworthy is the local mIoU indicator, where the method proposed in this paper reaches 57.6%, which is 10.7 percentage points higher than Mask2Former's 46.9%, representing a relative improvement of 22.8%. This verifies the significant gains of the deformation-robust attention mechanism and edge contrast loss in the segmentation of damaged areas. The F1-score reaches 72.8%, indicating that the missed detections and false detections in component-level detection have been effectively suppressed. Figure 1 shows the precision-recall curves of each method at different IoU thresholds. The x-axis represents the recall rate, and the y-axis represents the precision rate. The larger the area under the curve, the better the comprehensive performance.

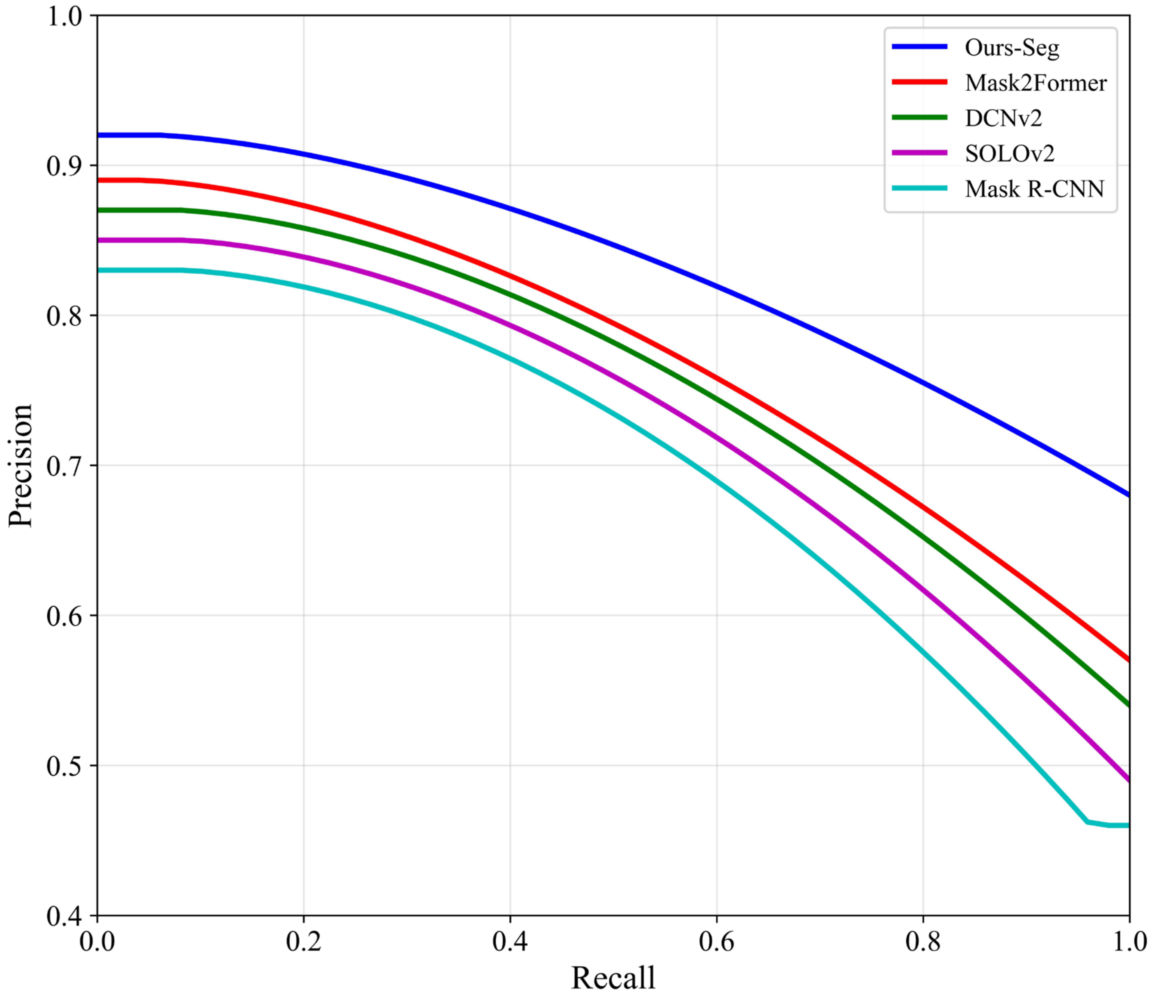

Figure 1. Precision-recall curves of different methods in the task of identifying the forms of discarded products

The method described in this paper (the solid line) is consistently higher than the comparison curve throughout the recall rate range. Particularly, in the recall rate range of 0.6 to 0.8, the accuracy rate remains above 75% steadily, while Mask2Former drops to around 68% in the same range.

5.3 Potential assessment experiment

To verify the effectiveness of the proposed potential assessment module, two types of evaluation tasks — regression and classification — were designed. The regression task uses the mean absolute error (MAE) and Spearman rank correlation coefficient (ρ) between the potential prediction vector $\hat{p}$ and the expert true values p as the core indicators, defined as follows:

$$\mathrm{MAE} = \frac{1}{3N_t} \sum_{i=1}^{N_t} \sum_{k=1}^{3} | p_{i,k} - \hat{p}_{i,k} | \tag{11}$$

$$\rho = 1 - \frac{6\sum_{i=1}^{N_t} d_i^2}{N_t(N_t^2 - 1)}, d_i = \mathrm{rank}(\bar{p}_i) - \mathrm{rank}(\hat{\bar{p}}_i) \tag{12}$$

Here, N_t represents the number of samples in the test set, $\bar{p}_i$ and $\hat{\bar{p}}_i$ respectively denote the true average potential and the predicted average potential of the i-th sample, and rank(·) represents the ranking function. The classification task employs the three-class accuracy (Acc@3) and the macro-average F1 (Macro-F1). The comparison methods include: MLP regression using only global image features, a potential predictor that uses shape recognition output but does not include graph neural networks (Ours w/o GNN), a version that uses only graph neural networks but does not include cross-modal fusion (Ours w/o CMF), and the complete model (Ours-Full). All evaluations are conducted on 2,569 images in the test set, and the results are listed in Table 3.

Table 3. Performance comparison of potential assessment tasks

Method	MAE (↓)	Spearman ρ (↑)	Acc@3 (%)	Macro-F1 (%)
MLP baseline	0.187 ± 0.012	0.621 ± 0.023	58.3 ± 1.5	56.7 ± 1.6
Ours w/o GNN	0.134 ± 0.009	0.743 ± 0.018	67.5 ± 1.2	66.1 ± 1.3
Ours w/o CMF	0.128 ± 0.010	0.761 ± 0.019	69.2 ± 1.3	67.8 ± 1.4
Ours-Full	0.106 ± 0.007	0.812 ± 0.015	74.6 ± 1.0	73.5 ± 1.1

The complete model achieved an MAE score of 0.106, indicating that the average prediction error for each potential indicator was approximately 10.6 percentage points, which was 43.3% lower than the MLP baseline. The Spearman correlation coefficient of 0.812 indicates a high degree of consistency between the model's predicted potential ranking and the expert ranking, ap $y = x$ proaching the upper limit of reproducibility for manual annotation (the inter-expert consistency is approximately 0.85). The classification accuracy was 74.6%, and it performed robustly for the three-class imbalanced problem. Figure 2 shows the scatter plot of the model's predicted potential and the experts' true potential, with the x-axis representing the true expert score and the y-axis representing the model's predicted value. Each point represents a test sample. The density of points near the diagonal $(y = x)$ reflects the prediction accuracy.

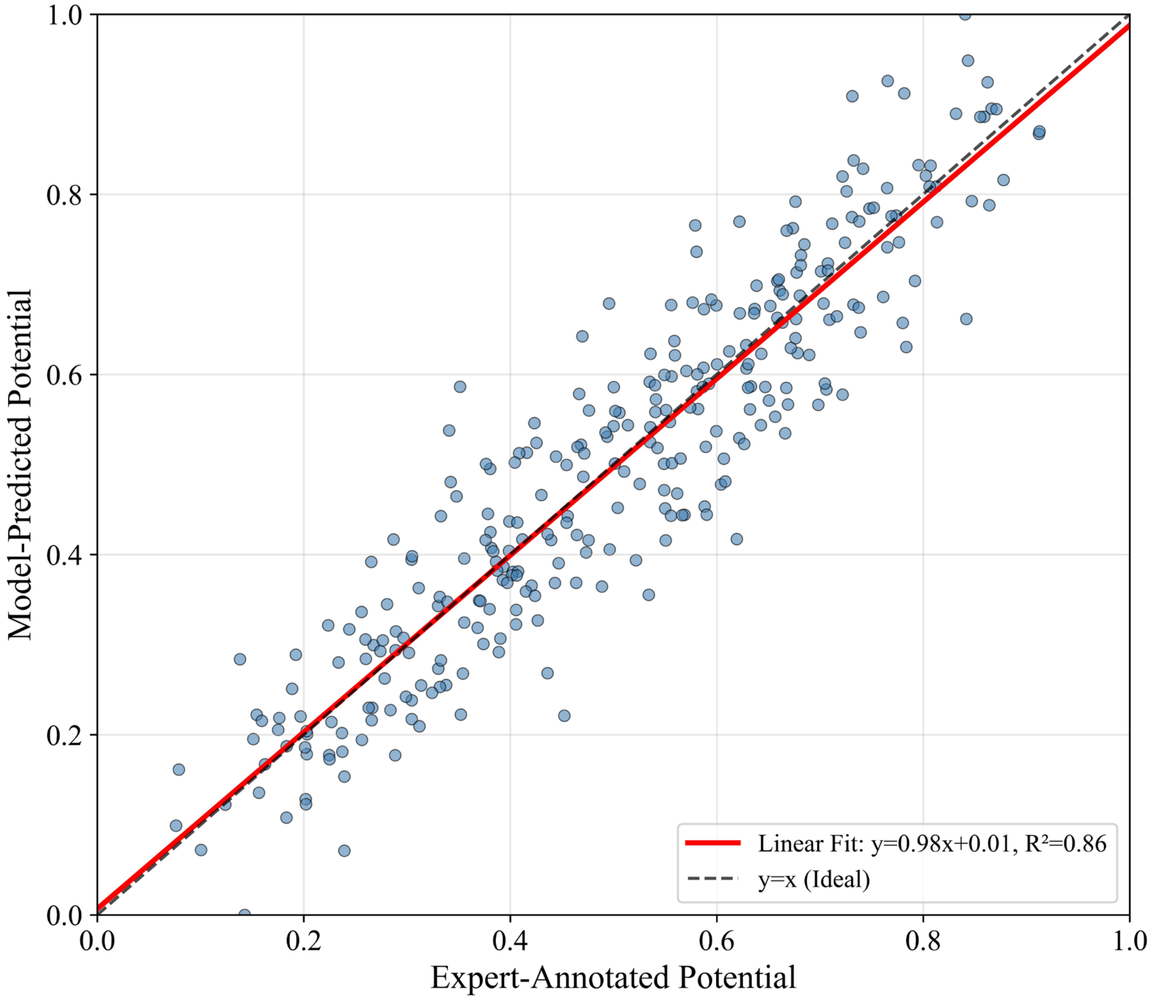

Figure 2. Scatter plot and linear fitting of the predicted potential of the model and the actual potential of the experts

From Figure 2, it can be seen that the sample points in the low-potential area (<0.4) and the medium-potential area (0.4-0.7) are closely distributed along the diagonal, while the high-potential area (>0.7) is slightly scattered but still shows a linear overall trend. The slope obtained by linear regression fitting is 0.98, the intercept is 0.01, and the R^2 value is 0.86. This indicates that the model has good consistency deviation control over the full range of potential calibration.

5.4 Ablation experiments

To quantify the independent contributions of each innovative module, a system-wide ablation experiment was designed. Starting from a base version (Base), which uses the standard ResNet-50-FPN backbone, no deformation-robust attention, no shape structure preservation loss or edge contrast loss, and the ordinary multi-task summation loss. Each module is gradually added: transformation robustness attention (DRA), shape structure preservation loss ($\mathcal{L}_{\text{shape}}$), edge contrast loss ($\mathcal{L}_{\text{edge}}$), graph neural network module (GNN), cross-modal fusion (CMF), and gradient coordination and uncertainty weighting (GCUW). All variants run under the same dataset and training strategy, and the recorded mIoU of shape recognition and MAE of potential assessment on the test set are presented in Table 4.

Table 4. Results of ablation experiments on the contribution of each module

Configuration	mIoU (%)	local mIoU (%)	MAE (↓)	Spearman ρ
Base	54.3	38.1	0.162	0.671
Base + DRA	58.9 (+4.6)	46.2 (+8.1)	0.148 (-0.014)	0.712 (+0.041)
Base + DRA + $\mathcal{L}_{\text{shape}}$	61.1 (+2.2)	49.8 (+3.6)	0.139 (-0.009)	0.736 (+0.024)
Base + DRA + $\mathcal{L}_{\text{shape}}$ + $\mathcal{L}_{\text{edge}}$	63.4 (+2.3)	54.3 (+4.5)	0.128 (-0.011)	0.754 (+0.018)
Base + all recogn. improv.	64.8 (+1.4)	56.1 (+1.8)	0.122 (-0.006)	0.768 (+0.014)
+ GNN	65.3 (+0.5)	56.8 (+0.7)	0.114 (-0.008)	0.792 (+0.024)
+ CMF	65.9 (+0.6)	57.2 (+0.4)	0.109 (-0.005)	0.805 (+0.013)
+ GCUW (Full)	66.2 (+0.3)	57.6 (+0.4)	0.106 (-0.003)	0.812 (+0.007)

The ablation results show that the Deformation Robustness Attention (DRA) contributes the most to the performance improvement, with a single module gain of 8.1 percentage points for local mIoU, confirming its crucial role in handling damaged and deformed samples. In terms of the loss function, the shape structure preservation loss and edge contrast loss have a complementary effect: the former improves the global clustering quality (mIoU increases by 2.2%), while the latter enhances the capture of boundary details (local mIoU increases by 4.5%). The graph neural network module and cross-modal fusion have limited gains for the recognition task (total mIoU improvement of 1.1%), but have a significant impact on the potential assessment task, with MAE reduced by 0.013 and Spearman ρ increased by 0.037, indicating that component relationship modeling has an irreplaceable value for potential prediction. Gradient coordination and uncertainty weighting provide stable small increments in various indicators, verifying the effectiveness of the multi-task optimization strategy.

5.5 Robustness test

To evaluate the model's generalization ability in real industrial scenarios, three sets of robustness tests were designed: increasing damage degree, increasing occlusion ratio, and varying lighting conditions. The damage degree was quantified by the ratio $r_{\text{damage}} = \text{Area}(\Omega_{\text{damage}})/\text{Area}(\Omega)$, ranging from 0.05 to 0.40 with a step of 0.05. For each damage level, at least 200 images were selected or synthesized from the test set for evaluation. The occlusion test used a similar scheme, with the occlusion ratio being the ratio of the occluder area to the product area, ranging from 0.1 to 0.6. Lighting variation was achieved by changing the image brightness factor (0.3× to 2.0×) and contrast factor (0.5× to 1.8×) in combination. Figure 3 shows the performance degradation curves of the complete model (Ours-Full) and the strongest baseline Mask2Former under different damage degrees and occlusion ratios, where the vertical axis represents the relative performance retention rate, defined as the current condition's mIoU divided by the mIoU in the no-damage condition.

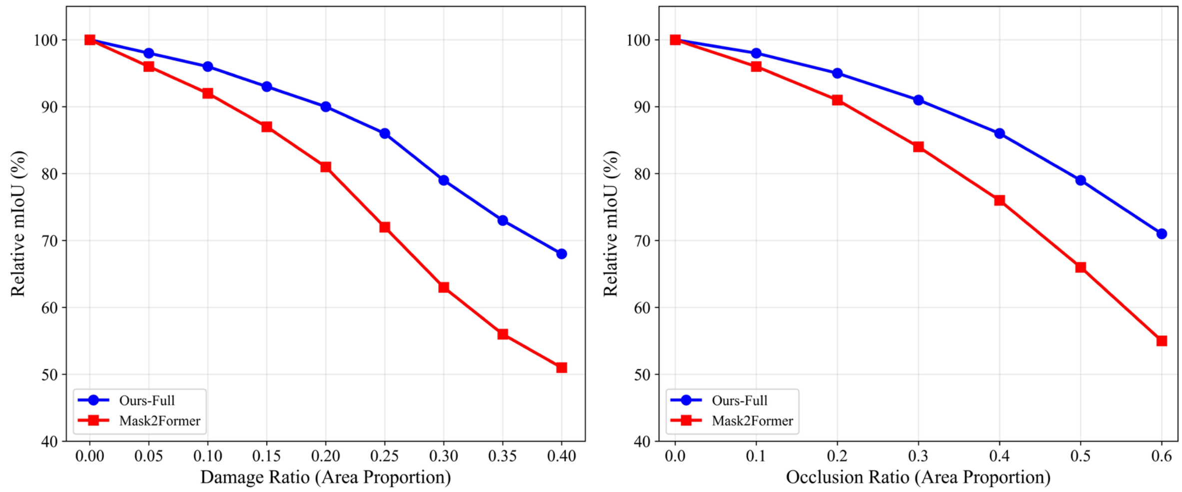

Figure 3. Comparison of model robustness under different damage and occlusion conditions

From the damage test curve in Figure 3 (left), it can be seen that when the damage ratio is lower than 0.15, the performance retention rate of our model remains above 95%, showing no significant difference from the baseline model. When the damage ratio rises to 0.25, the performance retention rate of the baseline model drops to 72%, while the model in this study still maintains a relative performance of 86%, demonstrating a strong tolerance to a wide range of damages. When the damage ratio reaches 0.40, the performance retention rate of the model in this study is 68%, significantly better than the 51% of the baseline model. The occlusion test in Figure 3 (right) shows a similar trend: at an occlusion ratio of 0.4, the relative performance of the model in this study is 79%, while the baseline is 61%; at an occlusion ratio of 0.5, the model in this study drops to 71%, and the baseline drops to 52%. This indicates that the deformation robustness attention mechanism effectively avoids semantic pollution caused by occluders by dynamically shifting the sampling points. In the illumination variation test (summarized in Table 5 in tabular form), the mIoU of the model in weak light (0.3× brightness) conditions drops to 81% of normal lighting conditions, while in strong light (2.0× brightness), it is 86%, while the corresponding values for the baseline model are 67% and 71%, further verifying the model's adaptability to changes in on-site acquisition conditions.

Table 5. Comparison of mIoU for morphological recognition under different lighting conditions

Lighting conditions	Brightness factor	Contrast factor	Ours-Full mIoU (%)	Mask2Former mIoU (%)
Normal lighting	1.0	1.0	66.2	62.4
Weak light	0.5	0.7	56.9 (86.0%)	49.3 (79.0%)
Extremely weak light	0.3	0.5	53.6 (81.0%)	41.8 (67.0%)
Strong light	1.8	1.4	59.8 (90.3%)	47.5 (76.1%)
Extremely strong light + overexposure	2.0	1.8	56.9 (86.0%)	44.3 (71.0%)

Note: The figures in parentheses represent the performance retention rate under relative to normal lighting conditions.

6. CONCLUSION AND OUTLOOK

This paper addresses the dual challenges of difficulty in form recognition and the lack of potential assessment in the scenario of redesigning discarded products by proposing an end-to-end deep learning joint model. In terms of form recognition, the designed multi-branch feature extraction structure and deformation-robust attention mechanism effectively overcome the common problems of bent distortion, local damage, and multi-scale mixture in discarded products. The introduction of form structure preservation loss and edge contrast loss further strengthens the boundary segmentation ability of damaged areas. Experiments show that this method improves the local intersection-over-union index of damaged areas by more than ten percentage points compared to the existing optimal model, proving its advantage in specialized modeling for irregular form degradation. In the potential assessment of re-design, a three-element index system of structural reusability, material integrity, and form modification freedom was constructed. The component relationship encoding module based on graph neural networks can capture the spatial attachment and connection topology information within the discarded product, and the form-potential joint embedding space realizes the interpretable mapping from geometric form to engineering potential. The parallel output design of potential regression and level classification takes into account both precise sorting and rapid screening, achieving a Spearman correlation coefficient of over 0.81 with the consistency of expert scoring, verifying the effectiveness of quantitative assessment.

From the perspective of engineering applicability, the model in this paper can be directly deployed in the image acquisition stage of the waste product recycling sorting line. Without the need for manual disassembly or physical inspection, it can output the component-level segmentation results and re-design potential scores of each product in real time. This capability provides quantitative decision-making basis for re-design engineers: high-potential products can enter the detailed disassembly and functional reconfiguration process, medium-potential products are suitable for material replacement or partial renovation, and low-potential products are redirected to the traditional material recycling path. Compared with the existing mode that relies entirely on manual visual screening, this model significantly improves sorting efficiency and evaluation consistency, and reduces the loss of misjudgment caused by subjective judgment differences. The model shows good robustness to different degrees of damage and occlusion, maintaining a relative performance of 86% even when the damage ratio reaches 25%. This indicates its potential to work stably in real recycling scenarios (product stacking, dirtiness, light changes).

Looking to the future, this model still has several expandable directions. In the aspect of few-shot learning, the current model relies on a certain scale of high-quality labeled data. However, in actual industrial scenarios, new types of waste products constantly emerge, and labeling costs are high. In the future, we can introduce meta-learning or contrastive pre-training strategies to enable the model to quickly adapt to unknown product categories with only a small amount of samples. In the aspect of domain generalization, the dataset of this paper mainly comes from consumer electronics. The product types, damage patterns and background conditions on the recycling lines show significant domain differences. We can study methods based on domain adaptation or domain randomization to reduce the performance degradation of the model across different recycling lines. In the aspect of closed-loop optimization, the current model belongs to open-loop prediction and lacks feedback signals from actual re-design results. If we can construct a data loop of “prediction - re-design - effect evaluation - model update”, allowing the model to continuously learn from real re-design success cases, it will further improve the long-term accuracy and industrial adaptability of potential assessment. In addition, extending potential assessment from discrete ternary indicators to interpretable diagnostic maps (such as indicating which component and what kind of damage limits the re-design freedom) will also be an important direction for promoting the practical application of the model.

Abbreviations

GNN, Graph Neural Network;

GAT, Graph Attention Network;

CNN, Convolutional Neural Network;

MLP, Multilayer Perceptron;

ResNet, Residual Network;

FPN, Feature Pyramid Network;

DCNv2, Deformable Convolutional Network version 2;

Mask R-CNN, Mask Region-based Convolutional Neural Network;

YOLACT, You Only Look At CoefficienTs;

SOLOv2, Segmenting Objects by Locations version 2;

Mask2Former, Masked-attention Mask Transformer;

SGD, Stochastic Gradient Descent;

IoU, Intersection over Union;

mIoU, mean Intersection over Union;

mAP, mean Average Precision;

AP, Average Precision;

TP, True Positive;

FP, False Positive;

FN, False Negative;

F1, F1-Score;

MAE, Mean Absolute Error;

Acc, Accuracy;

R^2, R-Squared;

ReLU, Rectified Linear Unit;

ELU, Exponential Linear Unit;

GPU, Graphics Processing Unit;

CPU, Central Processing Unit;

DRA, Deformation-Robust Attention;

CMF, Cross-Modal Fusion;

GCUW, Gradient Coordination and Uncertainty Weighting;

PCB, Printed Circuit Board.

Supplementary Material

Not applicable.

Appendix

Not applicable.

Ethics approval and consent to participate.

This study did not involve human participants, animal subjects, or any data requiring ethical approval. Therefore, ethics approval and consent to participate are not applicable.

Acknowledgements

The authors would like to thank the editors of this journal and all the anonymous reviewers who provided valuable comments on this work.

Competing interests

The authors declare that they have no financial or personal relationships that may have inappropriately influenced them in writing this article.

Author contributions

All authors have read and agreed to the published version of the manuscript. The author's contributions are specified as follows: **M.Y.:** Conceptualization, Methodology, Software, Validation, Formal analysis, Investigation, Data Curation, Writing – Original draft, Writing – Review & Editing, Visualization, Supervision, Project administration.

Funding information

The authors declare that no funds, grants, or other support were received during the preparation of this manuscript.

Data availability

The data that support the findings of this study are available upon request from the corresponding authors, **M.Y.**

Disclaimer

The views and opinions expressed in this article are those of the authors and are the product of professional research. It does not necessarily reflect the official policy or position of any affiliated institution, funder, agency, or that of the publisher. The authors are responsible for this article's results, findings, and content.

Declaration of AI and AI-assisted Technologies in the Writing Process

During the writing of this article, the author used ChatGPT for spelling and grammar checking. After using this tool, the author reviewed and edited the content as needed and assumes full responsibility for the final published content.

REFERENCES

[1] Dumée, L. F. (2022). Circular materials and circular design—review on challenges towards sustainable manufacturing and recycling. *Circular economy and sustainability*, *2*(1), 9-23. https://doi.org/10.1007/s43615-021-00085-2

[2] Mesa, J. A., & González-Quiroga, A. (2023). Development of a diagnostic tool for product circularity: a redesign approach. *Research in Engineering Design*, *34*(4), 401-420. https://doi.org/10.1007/s00163-023-00415-5

[3] Triguero, A., Moreno-Mondéjar, L., & Sáez-Martínez, F. J. (2023). Circular economy and firm performance: The influence of product life cycle analysis, upcycling, and redesign. *Sustainable Development*, *31*(4), 2318-2331. https://doi.org/10.1002/sd.2509

[4] Boy, G. A., Masson, D., Durnerin, É., & Morel, C. (2024). PRODEC for human systems integration of increasingly autonomous systems. *Systems engineering*, *27*(5), 805-826. https://doi.org/10.1002/sys.21751

[5] Yan, Y., Tong, L., Song, K., Tian, H., Man, Y., & Yang, W. (2023). SISG-Net: Simultaneous instance segmentation and grasp detection for robot grasp in clutter. *Advanced Engineering Informatics*, *58*, 102189. https://doi.org/10.1016/j.aei.2023.102189

[6] Tian, H., Song, K., Tong, L., Man, Y., & Yan, Y. (2023). Robot unknown objects instance segmentation based on collaborative weight assignment RGB–depth fusion strategy. *IEEE/ASME Transactions on Mechatronics*, *29*(3), 2032-2043. https://doi.org/10.1109/tmech.2023.3327865

[7] Muhammad, K., Hussain, T., Ullah, H., Del Ser, J., Rezaei, M., Kumar, N., ... & De Albuquerque, V. H. C. (2022). Vision-based semantic segmentation in scene understanding for autonomous driving: Recent achievements, challenges, and outlooks. *IEEE Transactions on Intelligent Transportation*

Systems, *23*(12), 22694-22715. https://doi.org/10.1109/tits.2022.3207665

[8] Dumée, L. F. (2022). Circular materials and circular design—review on challenges towards sustainable manufacturing and recycling. *Circular economy and sustainability*, *2*(1), 9-23. https://doi.org/10.1007/s43615-021-00085-2

[9] Strzelecka, C. (2024). Critical data studies meets discard studies: Waste data reflectivity in digital urban waste tracking system. *Convergence*, *30*(6), 2109-2130. https://doi.org/10.2139/ssrn.4981045

[10] Zhang, X., Song, Y., Song, T., Yang, D., Ye, Y., Zhou, J., & Zhang, L. (2024). LDConv: Linear deformable convolution for improving convolutional neural networks. *Image and Vision Computing*, *149*, 105190. https://doi.org/10.48550/arXiv.2311.11587

[11] Gao, F., Cai, C., Tang, W., Tian, Y., & Huang, K. (2024). RA2DC-Net: A residual augment-convolutions and adaptive deformable convolution for points-based anchor-free orientation detection network in remote sensing images. *Expert Systems with Applications*, *238*, 122299. https://doi.org/10.1016/j.eswa.2023.122299

[12] Ravichandran, B., Boissie, K., & Madhavan, P. (2025). A multidimensional methodological approach to disassembly index calculation: Enhancing product dismountability and sustainability. *Sustainable Production and Consumption*, *56*, 80-93. https://doi.org/10.1016/j.spc.2025.03.016

[13] Glas, M., Kersten, L., Mulders, T., Pernul, G., & Allodi, L. (2026, April). T1GER: An Instructional Re-Design of a Cyber Range Exercise in a Commercial Security Operations Center. In *Proceedings of the 2026 CHI Conference on Human Factors in Computing Systems* (pp. 1-22). https://doi.org/10.1145/3772318.3791226

[14] Orso, V., Ziviani, R., Bacchiega, G., Bondani, G., Spagnolli, A., & Gamberini, L. (2022). Employee-centric innovation: Integrating participatory design and video-analysis to foster the transition to Industry 5.0. *Computers & Industrial Engineering*, *173*, 108661. https://doi.org/10.1016/j.cie.2022.108661

[15] Hercog, D., Bencak, P., Vincetič, U., & Lerher, T. (2022). Product assembly assistance system based on pick-to-light and computer vision technology. *Sensors*, *22*(24), 9769. https://doi.org/10.3390/s22249769

[16] Wang, Y., Peng, X., Huang, W., Ye, X., & Jiang, M. (2023). Self-supervised non-rigid structure from motion with improved training of Wasserstein GANs. *IET Computer Vision*, *17*(4), 404-414. https://doi.org/10.1049/cvi2.12175

[17] Ghoul, A., Pan, J., Lingg, A., Kübler, J., Krumm, P., Hammernik, K., ... & Küstner, T. (2024). Attention-aware non-rigid image registration for accelerated MR imaging. *IEEE transactions on medical imaging*, *43*(8), 3013-3026. https://doi.org/10.1109/tmi.2024.3385024

[18] Zhu, D., Wang, W., Xue, X., Xie, H., Cheng, G., & Wang, F. L. (2024). Structure-preserving image smoothing via contrastive learning. *The Visual Computer*, *40*(8), 5139-5153. https://doi.org/10.1007/s00371-023-02897-9

[19] Pan, S., Pu, Y., Zhao, Z., Yang, Q., Gu, J., & Xu, D. (2025). StrCCL: Structure-Aware Contrastive Consistency Loss for Artistic Style Transfer. *Expert Systems with Applications*, 129901. https://doi.org/10.1016/j.eswa.2025.129901

[20] Cao, Z., Huang, Y., Zhou, Y., Zhou, P., & He, Y. (2025). GlogSemiFNet: a semi-supervised contrastive learning framework for high-resolution remote sensing farmland edge detection based on frequency domain filters. *Geo-spatial Information Science*, 1-25. https://doi.org/10.1080/10095020.2025.2589636

[21] Ruschhaupt, S., Troles, J., & Schmid, U. M. (2025). Comparing Mask R-CNN and Mask2Former architectures for individual tree crown delineation. https://doi.org/10.18420/giljt2025_13

[22] Alshawabkeh, S., Wu, L., Dong, D., Cheng, Y., & Li, L. (2025). A hybrid approach for pavement crack detection using mask R-CNN and vision transformer model. *Computers, Materials, & Continua*, *82*(1), 561. https://doi.org/10.32604/cmc.2024.057213

[23] Shanmugasundaram, S., & Palaniappan, N. (2024). Improvement of Bounding Box and Instance Segmentation Accuracy Using ResNet-152 FPN with Modulated Deformable ConvNets v2 Backbone-based Mask Scoring R-CNN. *International Journal of Image and Graphics*, *24*(06), 2450054. https://doi.org/10.1142/s0219467824500542

[24] Mesa, J. A., & González-Quiroga, A. (2023). Development of a diagnostic tool for product circularity: a redesign approach. *Research in Engineering Design*, *34*(4), 401-420. https://doi.org/10.1007/s00163-023-00415-5

[25] Fanicchia, F., & Karlsdottir, S. N. (2023). Research and development on coatings and paints for geothermal environments: A review. *Advanced Materials Technologies*, *8*(18), 2202031. https://doi.org/10.1002/admt.202202031

[26] Ferrero, V., DuPont, B., Hassani, K., & Grandi, D. (2022). Classifying component function in product assemblies with graph neural networks. *Journal of Mechanical Design*, *144*(2), 021406. https://doi.org/10.1115/1.4052720

[27] Jian, C., Lu, Y., Lin, M., & Zhang, M. (2023). A novel graph neural networks approach for 3D product model retrieval. *International Journal of Computer Integrated Manufacturing*, *36*(3), 381-392. https://doi.org/10.1080/0951192x.2022.2104460

[28] Murat, A., & Ali, S. (2024). Low-resource POS tagging with deep affix representation and multi-head attention. *IEEE Access*, *12*, 66495-66504. https://doi.org/10.1109/access.2024.3395454

[29] Sivaramakrishnan, J., Lee, G., Parlevliet, D., & Wong, K. W. (2022). Margin-based approach for outlier detection of industrial design data using a modified general regression neural network. *AI EDAM*, *36*, e7. https://doi.org/10.1017/S0890060421000329

[30] Jadon, A., Patil, A., & Jadon, S. (2024, January). A comprehensive survey of regression-based loss functions for time series forecasting. In *International Conference on Data Management, Analytics & Innovation* (pp. 117-147). Singapore: Springer Nature Singapore. https://doi.org/10.1007/978-981-97-3245-6_9

[31] Shi, Z., Yao, W., Zhao, Y., Ai, X., Wen, J., & Cheng, S. (2024). Two-stage weakly supervised learning to mitigate label noise for intelligent identification of power system dominant instability mode. *Applied Energy*, *359*, 122659. https://doi.org/10.1016/j.apenergy.2024.122659

[32] Ye, Z., Wang, X., & Cai, Z. (2025). Performance Evaluation and Optimization of Multi-stage Manufacturing Systems: A Review. *Reliability Analysis and Maintenance Optimization of Complex Systems: Essays in Honor of Professor Won Young Yun on his 65th Birthday*, 211-243.

https://doi.org/10.1007/978-3-031-70288-4_13

[33] Nath, D., Ankit, Neog, D. R., & Gautam, S. S. (2024). Application of Machine Learning and Deep Learning in Finite Element Analysis: A Comprehensive Review: D. Nath et al. *Archives of computational methods in engineering*, *31*(5), 2945-2984. https://doi.org/10.1007/s11831-024-10063-0

[34] Aliferis, C., & Simon, G. (2024). Overfitting, underfitting and general model overconfidence and under-performance pitfalls and best practices in machine learning and AI. *Artificial intelligence and machine learning in health care and medical sciences: Best practices and pitfalls*, 477-524. https://doi.org/10.1007/978-3-031-39355-6_10

[35] Pinto, A. H., Lounis, C., Causse, M., & Chanel, C. P. (2025). Online Metrics to Enhance Human-Artificial Agent Collaboration Efficiency: A Narrative Literature Review. *International Journal of Human–Computer Interaction*, 1-24. https://doi.org/10.1080/10447318.2025.2575895

APA Citation

Yang, M. (2026). A Model for Identifying the Forms of Discarded Products and Assessing Their Redesign Potential Based on Deep Learning. *International Scientific Technical and Economic Research, 4(3),* 22-43. **https://doi.org/10.67541/ISTAER2624**